

Synergistic Interface and Mesopore Engineering with More and Quicker Ion Storage for Enhanced Performance of Lithium-Ion Battery

Juan Li⁺^[a, b] Shuang Hou⁺^[a, b] Tiezhong Liu,^[a, b] Chen Mei,^[a, b] Liangke Wang,^[a, b] Jianing Wang,^[b] and Lingzhi Zhao^{*[a, b, c]}

Designing hetero-nanostructures is widely recognized as an effective modification strategy to obtain ZnO/Co₃O₄ anode materials with superior electrochemical properties. However, the lithium-ion storage behavior of ZnO/Co₃O₄ has not reached a satisfied performance. Herein, based on our previous DFT results that the interface of ZnO(110)/Co₃O₄(220) hetero-nanostructure possesses fast reaction kinetics because of more negative surface adsorption energy and lower diffusion barrier energy of lithium ions, we developed ZnO(110)/Co₃O₄(220)@C hetero-nanostructures with both abundant interfaces and uniform mesopores structure derived from 2D MOF precursor. Especially, ZnO/Co₃O₄@C hybrid materials with ZnO(110)/Co₃O₄(220) hetero-nanostructure show strong electronic inter-

actions and the widen distance of the crystal plane at the interface, resulting in stable hetero-nanostructures with faster ion diffusion channel and more active sites. Moreover, this material possesses uniform mesopores and 2D structure, which enables quicker transport capability and cycling longevity for lithium-ion storage. Impressively, when ZnO/Co₃O₄@C was used as anodes in lithium-ion batteries, the electrodes deliver improved initial specific capacities (1,630.5 and 1,496.9 mAh g⁻¹ at 0.2 and 0.5 Ag⁻¹), excellent capacity retention (1,758.3 mAh g⁻¹ after 370 cycles at 0.2 Ag⁻¹, and 607.7 mAh g⁻¹ up to 650 cycles at 5 Ag⁻¹), and superior rate capacity (937 and 468 mAh g⁻¹ at 1.0 and 5.0 Ag⁻¹ after 360 cycles).

1. Introduction

To date, rechargeable batteries have accounted for a large proportion of energy storage and have brought convenience to humans. LIBs (lithium-ion batteries) are considered as one of the most attractive options due to the advantages of ultra-high specific capacity and long cycle life. In the case of the development and rise of the LIBs industry, anode materials play a decisive role.^[1-3] Among various anode materials, TMOs (transition metal oxides) (e.g., Fe₂O₃, NiO, Co₃O₄, and ZnO) have attracted much attention due to their easy availability, high energy density, and rich redox chemistry. Moreover, the theoretical specific capacity of TMO is 2 to 3 times that of commercial graphite (\approx 372 mAh g⁻¹).^[4] Given the above advantages, abundant resources, low cost, and environmental

friendliness, ZnO/Co₃O₄ composite materials have been widely studied as one of the important alternative anodes for LIBs. However, the semi-conduct nature of ZnO/Co₃O₄ composite results in their slow electrochemical reaction kinetics with unsatisfactory electrochemical performance. Note that thoughtful designs, such as morphology, heterostructure, and carbon-coating, can improve the electrochemical performance of ZnO/Co₃O₄ composites.^[5-7]

Constructing heterojunction defined as the interface between two different semiconductors with unequal forbidden bandwidth (E_F) can form band alignment.^[8,9] The interfacial effect caused by the band alignment strategy greatly improves the overall kinetics of the electrochemical reactions and the lithium-ion storage performance of electrodes.^[10-12] In this context, constructing ZnO/Co₃O₄ heterostructures has been intensively reported. Chen et al. fabricated ZnO(101)/Co₃O₄(111) heterostructures attaching to the surface of carbon cloth (CC). At the current of 2,000 mA g⁻¹, ZnO-Co₃O₄@CC nanosheets exhibit a reversible capacity of 491 mAh g⁻¹ after 400 cycles.^[13] Fang et al. rationally used a facile strategy to fabricate ZnO(100)/Co₃O₄(400) composite, which can remain the specific capacity of 442 mAh g⁻¹ after 1,000 cycles at the current of 2,000 mA g⁻¹.^[14] Zhu et al. prepared ZnO(101)/Co₃O₄(220) nanocomposite clusters by a self-assembled strategy. The discharge capacity of ZnO(101)/Co₃O₄(220) nanocomposite gradually increases to 957 mAh g⁻¹ during 100 cycles at 100 mA g⁻¹.^[15] Nevertheless, the lithium-ion storage performance of the others interfacial regions between ZnO/Co₃O₄ is still unclear. Moreover, the electrochemical performance of ZnO/Co₃O₄ hetero-nanostructures needs to be improved.

[a] J. Li,⁺ S. Hou,⁺ T. Liu, C. Mei, L. Wang, Prof. L. Zhao
Guangdong Provincial Engineering Technology Research Center for Low Carbon and Advanced Energy Materials
Institute of Semiconductor Science and Technology
South China Normal University
Guangzhou 510631, China
E-mail: lzzhao@vip.163.com

[b] J. Li,⁺ S. Hou,⁺ T. Liu, C. Mei, L. Wang, J. Wang, Prof. L. Zhao
Institute of Science and Technology Innovation (Qingyuan)
South China Normal University
Guangzhou 510631, China

[c] Prof. L. Zhao
SCNU Qingyuan Institute of Science and Technology Innovation Co., Ltd.
Qingyuan 511517, China

[+] These authors contributed equally to this work.

 Supporting information for this article is available on the WWW under <https://doi.org/10.1002/batt.202100151>

The 2D porous structure and heterojunction engineering have been combined to achieve advanced applications, especially the uniform mesopores structure derived from 2D MOF.^[16–21] Herein, motivated by our previous result that ZnO(110)/Co₃O₄(220) hetero-structures [see Figure 1(a)] possess fast reaction kinetics due to the negative surface adsorption energy and lower diffusion barrier energy of lithium ions [see Figures 1(b), S1 and Table S1], we synthesize ZnO(110)/Co₃O₄(220) hetero-nanostructures with abundant interfaces and mesopores coated by carbon frameworks (ZnO(110)/

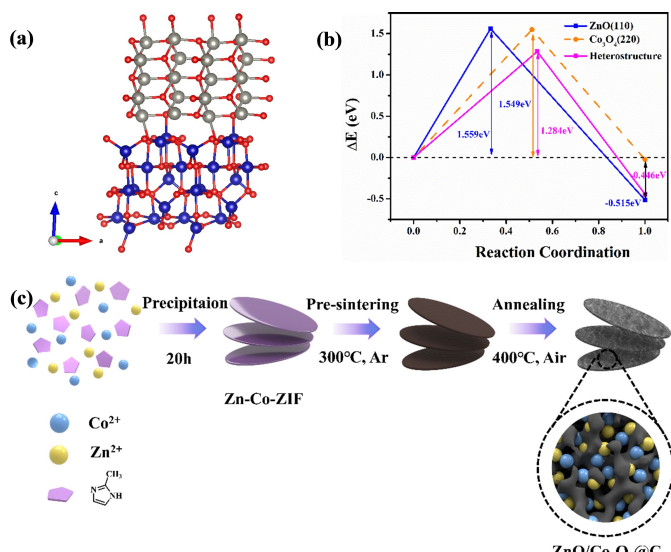


Figure 1. a) ZnO(110)/Co₃O₄(220) heterostructure model, b) the migration barriers to Li⁺ in bare ZnO(110), bare Co₃O₄(220) and ZnO(110)/Co₃O₄(220) hetero-nanostructure, c) schematic illustration of the synthesis process of ZnO/Co₃O₄@C hybrids.

Co₃O₄(220)@C derived from 2D zeolitic imidazolate frameworks (ZIFs) [see Figure 1(c)]. The obtained ZnO(110)/Co₃O₄(220)@C hybrid materials have the following advantages: (1) Transition metal oxides/carbon composites as anodes can achieve great electrochemical performance because carbon layers possess a strong volume buffering ability for composites and improve the conductivity of composites. (2) The hollow mesoporous structure can shorten the diffusion path of Li-ions and electrons, buffer volume change, increase the contact area between electrode and electrolyte, and facilitate more lithium-ion storage. (3) Interfacial engineering can accelerate the diffusion kinetics of lithium ions and provide more active sites for lithium-ion storage. (4) The synergistic effect of porous structure and interfacial engineering also can mitigate the volume expansion of composites.^[7–9] After comparing the electrochemical performance of the reported ZnO/Co₃O₄@C nanostructures as anodes in LIBs (see Tables S2, S3), the ZnO(110)/Co₃O₄(220)@C hetero-nanostructures deliver the improved initial specific capacities (1,630.5 and 1,496.9 mAh g⁻¹ at 0.2 and 0.5 A g⁻¹), excellent capacity retention (1,758.3 mAh g⁻¹ after 370 cycles at 0.2 A g⁻¹, 1,651.5 mAh g⁻¹ after 300 cycles at 0.5 A g⁻¹, and 607.7 mAh g⁻¹ up to 650 cycles at 5 A g⁻¹), and superior rate performance (937 and 468 mAh g⁻¹ at 1.0 and 5.0 A g⁻¹ after 360 cycles).

2. Results and Discussion

The crystal structure and phase purity of the ZnO/Co₃O₄@C hybrid are detected by XRD. In Figure 2(a), all diffraction peaks of ZnO/Co₃O₄@C exactly match with the hexagonal ZnO phase (JCPDS No. 89-1397) and cubic Co₃O₄ phase (JCPDS No. 74-2120) [4]. Some peaks located at 31.31°, 36.81°, 44.85°, 59.19°,

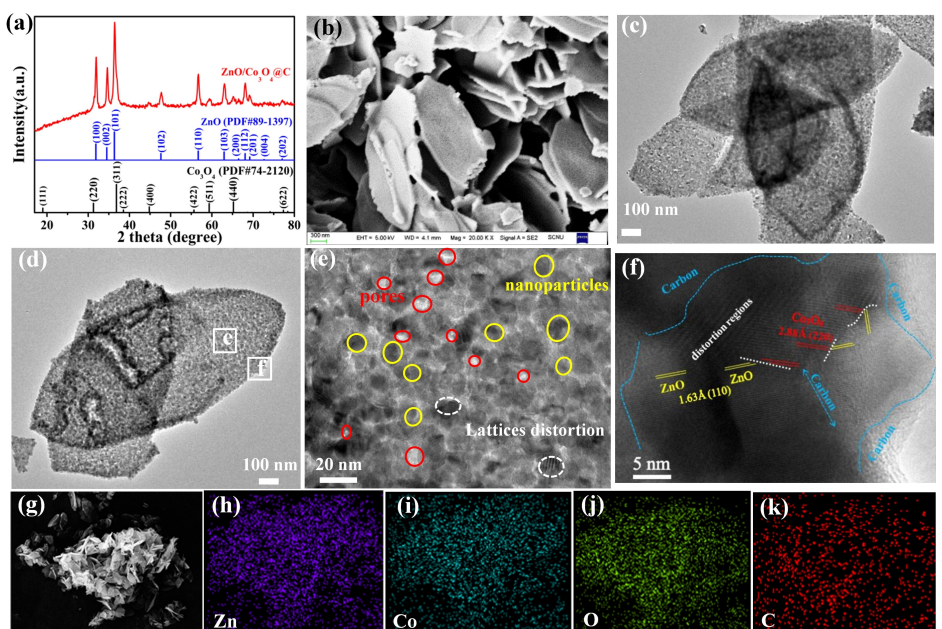


Figure 2. a) XRD pattern, b) FESEM, c–e) TEM, f) HRTEM of ZnO/Co₃O₄@C hybrid. g) SEM of ZnO/Co₃O₄@C hybrid and corresponding EDS mapping images of h) Zn, i) Co, j) O and k) C elements.

and 65.29° belong to (220), (311), (400), (511) and (440) planes of the Co_3O_4 phase, respectively. Other peaks centered at 32.09° , 34.84° , 36.51° , 47.98° , 56.87° , 63.24° , 66.83° , 68.21° , 69.37° and 77.11° are assigned to (100), (002), (101), (102), (110), (103), (200), (112), (201), and (202) crystal planes of ZnO , respectively. Figure S2(a) displays the XRD patterns of $\text{ZnO}@\text{C}$ and $\text{Co}_3\text{O}_4@\text{C}$ samples. Compared with the XRD of $\text{Co}_3\text{O}_4@\text{C}$, the (220), (511), and (400) lattice planes of $\text{ZnO}/\text{Co}_3\text{O}_4@\text{C}$ hybrid show a significant shift to lower 2θ degree [see Figure S2(b, c)]. The lattice spacing expansion and distortion of the Co_3O_4 phase in the $\text{ZnO}/\text{Co}_3\text{O}_4@\text{C}$ hybrid may be related to the doping of Zn atoms.

Figure S3 shows leaf-shaped structured of ZnCo-ZIF and pre-sintered ZnCo-ZIF , which are coated by thick carbon layers. Figure 2(b) displays $\text{ZnO}/\text{Co}_3\text{O}_4@\text{C}$ micro sheets with an average length of $\sim 1.5 \mu\text{m}$ and an average width of $\sim 700 \text{ nm}$. Figure 2(c and d) shows that hollow mesoporous $\text{ZnO}/\text{Co}_3\text{O}_4@\text{C}$ hybrid material is composed of $\text{ZnO}/\text{Co}_3\text{O}_4$ nanoparticles. Figure 2(e) presents the mesoporous structure (marked with red circles), the uniform distribution of $\text{ZnO}/\text{Co}_3\text{O}_4$ nanoparticles (yellow circles), and lattice distortion due to doping (white circles) in the $\text{ZnO}/\text{Co}_3\text{O}_4@\text{C}$ hybrid. HRTEM observation [see Figure 2(f)] provides the in-depth structural information of the $\text{ZnO}/\text{Co}_3\text{O}_4@\text{C}$ hybrid. Rich heterointerfaces (white dotted lines) with different orientations can achieve an interfacial effect, thereby improving the electrochemical performance of hybrids.^[22,23] The clear lattice fringes of ~ 2.88 and 1.63 \AA correspond to the (220) plane of Co_3O_4 and the (110) plane of ZnO , respectively. Some lattices show obvious distortion, and these distorted regions can buffer the stress of electrodes during electrochemical reactions. A large amount of carbon matrix (light blue dotted lines) can adapt to volume change and increase the conductivity of hybrids. Subsequently, EDS is measured by dispersing a $\text{ZnO}/\text{Co}_3\text{O}_4@\text{C}$ sample on the copper

foil. The EDS mapping images [see Figure 2(g-k)] show the uniform distribution of Zn (h), Co (i), O (j), and C (k) elements in the $\text{ZnO}/\text{Co}_3\text{O}_4@\text{C}$ hybrid.

The survey XPS spectrum [see Figure 3(a)] also manifests that $\text{ZnO}/\text{Co}_3\text{O}_4@\text{C}$ hybrid consists of Zn, Co, and O elements. Table S4 shows the XPS data of the element content. In the high-resolution XPS spectra of Zn 2p [see Figure 3(b)], the two peaks of $\text{ZnO}/\text{Co}_3\text{O}_4@\text{C}$ hybrid centered at 1,021.60 and 1,044.91 eV belong to the $2p_{3/2}$ and $2p_{1/2}$ of Zn 2p orbit level, respectively. Compared to the pure $\text{ZnO}@\text{C}$, the Zn 2p peaks of the $\text{ZnO}/\text{Co}_3\text{O}_4@\text{C}$ hybrid deliver a slight shift to higher binding energy, indicating that electrons are transferred from the ZnO phase to Co_3O_4 phase in $\text{ZnO}/\text{Co}_3\text{O}_4@\text{C}$.^[23] The fitting Co 2p spectrum of $\text{ZnO}/\text{Co}_3\text{O}_4@\text{C}$ hybrid [see Figure 3(c)] displays Co $2p_{3/2}$ (780.35 and 779.33 eV), Co $2p_{1/2}$ (769.05 and 794.45 eV), and satellite peaks (804.08 and 788.48 eV). These Co 2p peaks exhibit a clear shift to lower binding energy compared to pure $\text{Co}_3\text{O}_4@\text{C}$. It indicates that the electron cloud density around the Co_3O_4 phase in the $\text{ZnO}/\text{Co}_3\text{O}_4@\text{C}$ hybrid has increased significantly. Further, these apparent shifts in the binding energy of $\text{ZnO}/\text{Co}_3\text{O}_4@\text{C}$ hybrid indicate that the electrons of the Zn 2p state are transferred to the Co 2p state due to the formation of heterointerfaces, which confirms that strong electron interactions at heterointerfaces may promote Li-ions and electrons diffusion.^[22-24] The O 1s spectrum of $\text{ZnO}/\text{Co}_3\text{O}_4@\text{C}$ hybrid has three peaks [see Figure S4(a)]. An O3 peak at 532.05 eV stands for the metal-oxygen bond; another O2 peak at 530.72 eV is assigned to the oxygen vacancy; the last O1 centered at 529.13 eV is closely related to the surface adsorbed oxygen (OH^- , $\text{O}-\text{C}=\text{O}$, and H_2O).^[6,14] The high-resolution C1s spectrum [see Figure S4(b)] proves that the $\text{ZnO}/\text{Co}_3\text{O}_4@\text{C}$ hybrid contains amorphous/graphitic carbon (285.59 or 284.49 eV) and surface adsorbed carbon dioxide (288.53 eV).^[25-27]

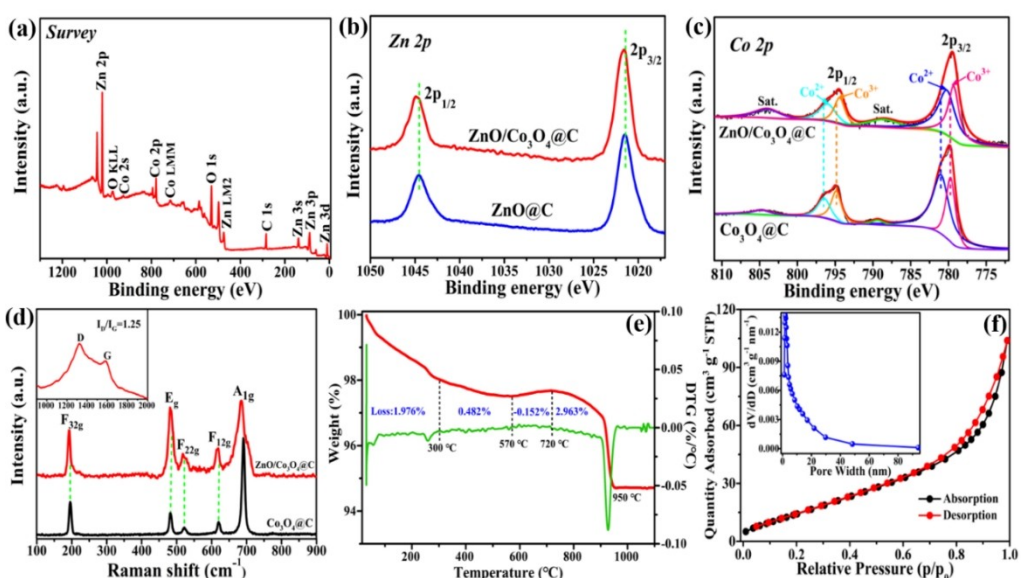


Figure 3. a) The survey XPS spectrum and elements information of $\text{ZnO}/\text{Co}_3\text{O}_4@\text{C}$, High-resolution XPS spectra of b) Zn 2p and c) Co 2p, d) Raman spectra. e) TGA/DTG curves, f) N_2 adsorption-desorption isotherms and pore width distribution curve of $\text{ZnO}/\text{Co}_3\text{O}_4@\text{C}$.

Co_3O_4 crystal composed of octahedral CoO_6 (Co^{3+} – O band) and tetrahedral CoO_4 (Co^{2+} – O band) is a typical spinel structured oxide. The Raman spectra of $\text{ZnO}/\text{Co}_3\text{O}_4@\text{C}$ and $\text{Co}_3\text{O}_4@\text{C}$ [see Figure 3(d)] show five vibration modes (A_{1g} , F_{12g} , F_{22g} , F_{32g} , and E_g), which are consistent with the mode of the spinel Co_3O_4 phase. In the Raman spectrum of $\text{Co}_3\text{O}_4@\text{C}$, the Raman response at 690 cm^{-1} corresponds to the A_{1g} mode related to the symmetrical stretching vibration of the Co^{3+} – O band. The Raman peak of CoO_4 stretching vibration at 195 cm^{-1} belongs to the F_{32g} mode. Besides, the peaks at 482 , 522 , and 621 cm^{-1} are ascribed to the active vibration modes of E_g , F_{22g} , and F_{12g} , respectively.^[28] However, the Raman modes of Co_3O_4 phase in the $\text{ZnO}/\text{Co}_3\text{O}_4@\text{C}$ hybrid are located at 686 cm^{-1} (A_{1g}), 616 cm^{-1} (F_{12g}), 518 cm^{-1} (F_{22g}), 481 cm^{-1} (E_g), and 192 cm^{-1} (F_{32g}), which have a significant redshift concerning $\text{Co}_3\text{O}_4@\text{C}$. It indicates that heterointerfaces are formed between the ZnO and Co_3O_4 phases in the $\text{ZnO}/\text{Co}_3\text{O}_4@\text{C}$ hybrids. The redshift phenomenon also occurs in the reported Raman spectra of graphene-Ag and MoS_2/C heterostructures.^[29]

No visible mode of the ZnO phase is observed in the Raman spectra of $\text{ZnO}/\text{Co}_3\text{O}_4@\text{C}$ [Figure 3(d)] and $\text{ZnO}@\text{C}$ [Figure S5(a)] due to the strong fluorescence effect of the ZnO phase. The photoluminescence of $\text{ZnO}@\text{C}$ is greatly stronger than that of $\text{Co}_3\text{O}_4@\text{C}$, but the photoluminescence of $\text{ZnO}/\text{Co}_3\text{O}_4@\text{C}$ is severely quenched. The photoluminescence of $\text{ZnO}/\text{Co}_3\text{O}_4@\text{C}$ is stronger than the pure $\text{Co}_3\text{O}_4@\text{C}$. Therefore, the photoluminescence of $\text{ZnO}/\text{Co}_3\text{O}_4@\text{C}$ is between the ZnO and Co_3O_4 phases [see Figure S4(c)]. The above phenomenon indicates that the heterointerfaces of $\text{ZnO}/\text{Co}_3\text{O}_4@\text{C}$ can speed up electrons transferring from the ZnO phase to the Co_3O_4 phase, thus increasing the electron cloud density around the Co_3O_4 phase of the $\text{ZnO}/\text{Co}_3\text{O}_4@\text{C}$ [23]. Figure 3(d) shows that the intensity ratio of the D band (amorphous carbon) and G band (graphitic carbon) is 1.25, suggesting that a large amount of amorphous carbon exists in the $\text{ZnO}/\text{Co}_3\text{O}_4@\text{C}$ hybrid.

The TGA analysis is performed on $\text{ZnO}/\text{Co}_3\text{O}_4@\text{C}$ to further determine the weight of carbon. In Figure 3(e), the weight loss of 1.976% belongs to adsorbed and coordinated water between 30 and 300°C . The increased weight of 0.152% may result from the enhanced crystallinity of ZnO and Co_3O_4 phases from 570 to 720°C , which can be demonstrated by the XRD patterns of $\text{ZnO}/\text{Co}_3\text{O}_4@\text{C}$ after annealing at 500 and 950°C [see Figure S5(b)].^[30–32] Thus, based on the TGA measurement from 300 to 1100°C , the carbon weight content of the $\text{ZnO}/\text{Co}_3\text{O}_4@\text{C}$ hybrid can be determined to be 3.29%. The results show that element C in the precursor disappears mainly in the form of surface-adsorbed carbon dioxide and exists sparingly in the form of carbon. According to the XPS data, the weight contents of ZnO and Co_3O_4 in the $\text{ZnO}/\text{Co}_3\text{O}_4@\text{C}$ are estimated to be 72.03 and 22.68% (94.71% in total), respectively. A large proportion of the ZnO phase contributes higher specific capacity to the $\text{ZnO}/\text{Co}_3\text{O}_4@\text{C}$ hybrid. Therefore, the theoretical specific capacity of $\text{ZnO}/\text{Co}_3\text{O}_4@\text{C}$ is calculated to be 918.5 mAh g^{-1} using “ $C_{\text{theoretical}} = C_{\text{ZnO}} \times \text{wt\% of ZnO} + C_{\text{C}} \times \text{wt\% of C} + C_{\text{Co}_3\text{O}_4} \times \text{wt\% of Co}_3\text{O}_4$ ”, where the theoretical capacities of all components are equal to 978 (C_{ZnO}), 890 ($C_{\text{Co}_3\text{O}_4}$) and 372 mAh g^{-1} (C_{C}), respectively.^[5,32]

The N_2 adsorption/desorption isotherms of $\text{ZnO}/\text{Co}_3\text{O}_4@\text{C}$ hybrid [see Figure 3(f)] with hysteresis loops can be indexed as type-IV isotherms based on IUPAC systematization, which clarifies the distribution of mesopores.^[15,33] The BET surface area of the $\text{ZnO}/\text{Co}_3\text{O}_4@\text{C}$ is $69.9\text{ m}^2\text{ g}^{-1}$, larger than those of $\text{ZnO}@\text{C}$ ($33.5\text{ m}^2\text{ g}^{-1}$) and $\text{Co}_3\text{O}_4@\text{C}$ ($37.6\text{ m}^2\text{ g}^{-1}$) [see Figure S5(a, b)], respectively. The large surface area can furnish sufficient active sites for Li-ions storage and provide a large amount of contact area between the active material and electrolyte. Figure 3(f) shows that the average pore size of $\text{ZnO}/\text{Co}_3\text{O}_4@\text{C}$ is 9.09 nm , and these pores are good for transporting Li-ions and electrons, buffering volume change, and enhancing contact area between the electrolyte and electrode.

The Mott-Schottky experiments show that the flat-band potentials of the $\text{ZnO}@\text{C}$ and $\text{Co}_3\text{O}_4@\text{C}$ electrodes are located at -0.19 and -0.22 V vs. Ag/AgCl, respectively [see Figure 4(a)]. The UV-vis diffusion reflection spectra exhibit that the absorbance of the $\text{ZnO}/\text{Co}_3\text{O}_4@\text{C}$ hybrid is significantly improved compared to $\text{ZnO}@\text{C}$ and $\text{Co}_3\text{O}_4@\text{C}$. The ultra-high absorbance may make $\text{ZnO}/\text{Co}_3\text{O}_4@\text{C}$ hybrid possess other potential applications [see Figure S6(a)]. The Kubelka-Munk plots [see Figure 4(b)] show that the bandgap values of $\text{ZnO}@\text{C}$ and $\text{Co}_3\text{O}_4@\text{C}$ are 3.68 and 2.11 eV , respectively. As a result, when the ZnO phase is assembled with the Co_3O_4 phase, a type-I heterojunction with band alignment forms.^[8,11,23] The E_f of the $\text{ZnO}/\text{Co}_3\text{O}_4@\text{C}$ hybrid greatly reduces, indicating the $\text{ZnO}/\text{Co}_3\text{O}_4@\text{C}$ hybrid with better conductivity [see Figure S6(c)]. The established type-I $\text{ZnO}/\text{Co}_3\text{O}_4$ hetero-nanostructure significantly accelerates the transport of electrons from the ZnO phase to the Co_3O_4 phase through heterointerfaces.

The conductivity of materials is further studied by Nyquist diagrams. The R_{ct} (charge-transfer resistance) of $\text{ZnO}/\text{Co}_3\text{O}_4@\text{C}$ is far lower than those of $\text{ZnO}@\text{C}$ and $\text{Co}_3\text{O}_4@\text{C}$ electrodes [see Figure 4(c)]. R_{ct} of $\text{ZnO}/\text{Co}_3\text{O}_4@\text{C}$ electrode after 40 cycles reaches a maximum and then gradually decreases during

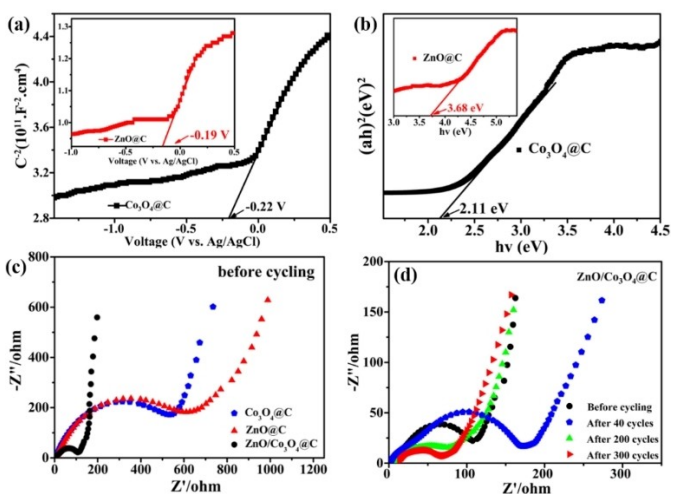


Figure 4. (a) Mott-Schottky plots of $\text{ZnO}@\text{C}$ and $\text{Co}_3\text{O}_4@\text{C}$, (b) Kubelka-Munk plots and (c) Nyquist plots of $\text{ZnO}@\text{C}$, $\text{Co}_3\text{O}_4@\text{C}$ and (d) $\text{ZnO}/\text{Co}_3\text{O}_4@\text{C}$ electrodes.

subsequent cycling [see Figure 4(d)]. D_{Li} of electrodes is expressed in the terms of Equations (1) and (2):^[42,45]

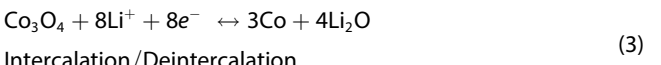
$$Z_{\text{re}} = R_s + R_{\text{ct}} + \sigma \omega^{-1/2} \quad (1)$$

$$D_{\text{Li}} = \frac{R^2 T^2}{2A^2 n^4 F^4 C^2 \sigma^2} \quad (2)$$

where Z_{re} is the real part of impedance; R_s the internal resistance of electrodes; ω , σ , R , and T are the angular frequency, Warburg coefficient, gas constant, and absolute temperature, respectively; A , n , F , and C the surface area of electrodes, the number of electrons, Faraday constant, and the concentration of Li-ions, respectively. σ can be obtained by the fit lines of $Z_{\text{re}} - \omega^{-1/2}$ [see Figure S6(b)], indicating that the D_{Li} of the fresh ZnO/Co₃O₄@C electrode ($6.5 \times 10^{-15} \text{ cm}^2 \text{s}^{-1}$) is bigger than these of Co₃O₄@C ($2.14 \times 10^{-16} \text{ cm}^2 \text{s}^{-1}$) and ZnO@C ($8.5 \times 10^{-17} \text{ cm}^2 \text{s}^{-1}$). Similarly, D_{Li} of the cycled ZnO/Co₃O₄@C electrodes are $5.8 \times 10^{-15} \text{ cm}^2 \text{s}^{-1}$ (after 40 cycles), $2.6 \times 10^{-13} \text{ cm}^2 \text{s}^{-1}$ (after 200 cycles) and $3.5 \times 10^{-13} \text{ cm}^2 \text{s}^{-1}$ (after 300 cycles), respectively. The feature of D_{Li} for ZnO/Co₃O₄@C electrodes is highly consistent with the cycling performance.

The electrochemical mechanism of ZnO/Co₃O₄@C hybrids is studied via CV curves and galvanostatic charge/discharge profiles. In Figure 5(a), the first discharge process of the ZnO/Co₃O₄@C electrode displays two distinct cathodic peaks at 0.63 V (I) and 0.42 V (II), respectively. The former is associated with the reduction of Co₃O₄ to Co [see Eq. (3)] and the formation of SEI (solid electrolyte interface) film; the latter is related to the reduction of ZnO to Zn [see Eq. (4)] and the alloying reaction of the subsequent Zn [see Eq. (5)].^[5,13,14] Three anodic peaks around 0.74, 1.60, and 2.08 V are discovered during the first charge process. The first peak near 0.74 V belongs to the dealloying reaction of Li-ions from Li-Zn alloys [see Eq. (5)]; the second wide peak centered at 1.60 V corresponds to the conversion of Zn to ZnO [see Eq. (4)]; the last peak located at 2.08 V is ascribed to the oxidation of Co to Co₃O₄ and the decomposition of the amorphous Li₂O [see Eq. (2)].^[34,35] As mentioned above, these peaks are only closely interrelated with the redox reactions of ZnO and Co₃O₄ phases, revealing no other miscellaneous phases in the ZnO/Co₃O₄@C hybrids. The CV curves of the ZnO@C and Co₃O₄@C electrodes (see Figure S7) are investigated at the same sweep rate of

0.2 mV s^{-1} at 0.01–3.0 V (vs. Li/Li⁺) to further analyze the electrochemical mechanism of ZnO/Co₃O₄@C.



The discharge-charge profiles of the ZnO/Co₃O₄@C hybrid are measured at a current density of 0.2 Ag^{-1} between 0.01 and 3.0 V vs. Li⁺/Li. Figure 5(b) shows an evident voltage plateau at ~ 0.70 V in the first discharge process and a peak at ~ 1.63 V in the first charge process. ZnO/Co₃O₄@C electrodes deliver the high initial discharge/charge specific capacities of $1,519.2$ and $1,116.4 \text{ mAh g}^{-1}$, respectively. The loss of reversible specific capacity may be closely related to the formation of SEI film and the incomplete conversion of electrochemical reactions. The discharge/charge capacities of the ZnO/Co₃O₄@C electrode after 300 cycles are $1,746.6$ and $1,726.1 \text{ mAh g}^{-1}$, respectively, indicating that ZnO/Co₃O₄@C electrode possesses superior cycling performance and higher capacity retention.

Figure 6(a) shows in the first 40 cycles, the ZnO/Co₃O₄@C electrode shows a first discharge specific capacity of $1,630.5 \text{ mAh g}^{-1}$ at 0.2 Ag^{-1} and average discharge specific capacities of $1,257.5$, $1,009.6$, 827.7 , 677.9 , 545.5 , and 465.0 mAh g^{-1} at different current densities of 0.2 , 0.5 , 1.0 , 2.0 , 3.0 , and 5.0 Ag^{-1} in the subsequent cycles, respectively. When the current density recovers to 0.2 Ag^{-1} , the discharge capacity can return to $1,003.3 \text{ mAh g}^{-1}$. After 360 cycles, the extremely high average rate capacities of the ZnO/Co₃O₄@C electrode are $1,757.2$, $1,543.7$, $1,243.2$, 937.0 , and 468.0 mAh g^{-1} at 0.2 , 0.4 , 0.6 , 1.0 , and 5.0 Ag^{-1} , respectively. When the current density returns to 0.2 Ag^{-1} again, the high specific capacity of $1,600.1 \text{ mAh g}^{-1}$ can still be maintained. The above analysis illustrates that the excellent rate performance of the ZnO/Co₃O₄@C hybrid is significantly better than previously reported Co₃O₄/ZnO composites (see Table S3).^[14]

Figure 6(b, c) shows the cycling performance curves of ZnO/Co₃O₄@C hybrids. Under the current density of 0.2 Ag^{-1} ,

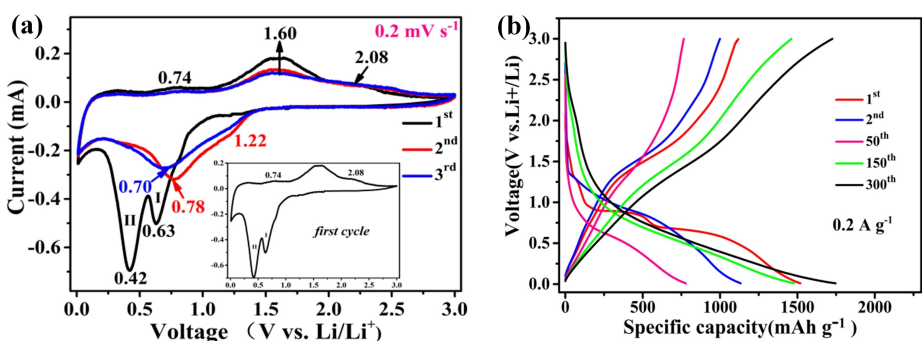


Figure 5. a) CV curves, b) charge and discharge profiles of ZnO/Co₃O₄@C electrode.

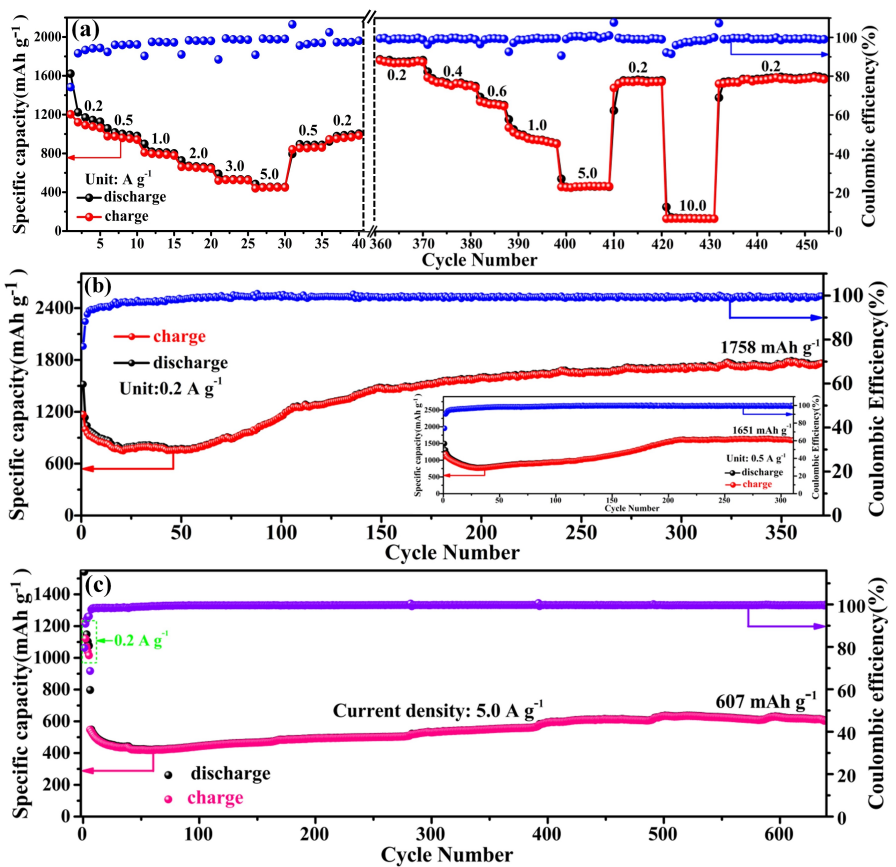


Figure 6. a) Rate capacities and cycling performance of $\text{ZnO}/\text{Co}_3\text{O}_4@\text{C}$ electrode at b) 0.2 A g^{-1} , (the inset of b) 0.5 A g^{-1} , and c) 5 A g^{-1} .

the $\text{ZnO}/\text{Co}_3\text{O}_4@\text{C}$ electrode delivers a high initial discharge and charge capacities of $1,519.2$ and $1,116.4 \text{ mAh g}^{-1}$, respectively. The first coulombic efficiency is approximately equal to 73.5% . The decrease in specific capacity can be assigned to the formation of the SEI film, the decomposition of electrolyte, and the incomplete conversion of the electrochemical reactions.^[36–40] More importantly, the $\text{ZnO}/\text{Co}_3\text{O}_4$ electrode shows an excellent discharge capacity of $1,133.2 \text{ mAh g}^{-1}$ and a higher capacity retention rate of 90.5% in the second cycle. Compared with $\text{ZnO}@\text{C}$ and $\text{Co}_3\text{O}_4@\text{C}$ electrodes, the $\text{ZnO}/\text{Co}_3\text{O}_4@\text{C}$ electrode has a long cycling life, high reversible specific capacity, and low capacity loss (see Figure S8). Next, the $\text{ZnO}/\text{Co}_3\text{O}_4@\text{C}$ electrode displays a low discharge capacity of 773.8 mAh g^{-1} in the 20th cycle, which can be traced to the unstable SEI film and volume change. The cycling performance of the $\text{ZnO}/\text{Co}_3\text{O}_4@\text{C}$ hybrid is relatively stable between 20 and 45 cycles, and then the specific capacity gradually increases from 45 to 200 cycles. The cycling performance finally maintains stability. Owing to the sluggish kinetics of the active materials, the increased capacity of the $\text{ZnO}/\text{Co}_3\text{O}_4@\text{C}$ hybrid may result from the reversible growth of polymer/gel-like film and electrode reactivation, related to the increased interfaces exposed by volume change and the pulverization of active materials. These exposed interfaces provide more active sites for lithium storage and accelerate the diffusion of lithium-ions and electrons. Meanwhile, $\text{ZnO}/\text{Co}_3\text{O}_4@\text{C}$ fragments can reduce

the diffusion path and impedance of lithium-ions and electrons.^[20,41–44] Even after 370 cycles, the $\text{ZnO}/\text{Co}_3\text{O}_4@\text{C}$ electrode can still maintain a high discharge capacity of $1,758.3 \text{ mAh g}^{-1}$ at 0.2 A g^{-1} .

Attractively, the excellent cycling performance of the $\text{ZnO}/\text{Co}_3\text{O}_4@\text{C}$ electrode also occurs at 0.5 A g^{-1} (see Figure 6b). The first discharge and charge capacities are $1,496.9$ and $1,110.5 \text{ mAh g}^{-1}$, respectively. Subsequently, the specific capacity reduces to 760.9 mAh g^{-1} in the 30th cycle and then stabilizes at $\sim 1,630 \text{ mAh g}^{-1}$. After 300 cycles, the specific capacity of the $\text{ZnO}/\text{Co}_3\text{O}_4@\text{C}$ electrode increases to $1,651.5 \text{ mAh g}^{-1}$ at 0.5 A g^{-1} . The cycling capacities of the $\text{ZnO}/\text{Co}_3\text{O}_4@\text{C}$ electrode are measured at 5 A g^{-1} during 650 cycles to evaluate the long-cycling performance (see Figure 6c). The high discharge capacity decreases to 418.7 mAh g^{-1} after 50 cycles. After 510 and 650 cycles, the reversible specific capacities are 635.0 and 607.7 mAh g^{-1} , respectively. The cycling performance of $\text{ZnO}/\text{Co}_3\text{O}_4@\text{C}$ electrodes at a large current density is more stable than that at a small current density. The activation time of the $\text{ZnO}/\text{Co}_3\text{O}_4@\text{C}$ electrode is shortened. The excellent electrochemical performance of the $\text{ZnO}/\text{Co}_3\text{O}_4@\text{C}$ electrode can be attributed to the following factors: i) The unique porous structure can buffer the volume change, shorten the diffusion path of Li-ions during electrochemical reactions, and enhance the effective contact area between electrolyte and electrode interface. ii) The synergistic

effect of mixed metal oxides can improve the conductivity of the electrode. iii) The interfacial effect can accelerate the diffusion kinetics of electrons and ions, enhance the electrochemical conductivity of hybrids due to band alignment, and contribute more active sites for lithium storage.

In Figure 7(a, b), the structure of ZnO/Co₃O₄@C hybrid after 300 cycles essentially remains intact, and the hybrid presents excellent electrical contact. The gradually exposed interfaces of ZnO/Co₃O₄ nanoparticles accelerate the slow kinetics of Li-ions/electrons, and the increased contact area provides more active sites for lithium ions storage. HRTEM images of ZnO/Co₃O₄@C electrodes before cycling [see Figure 2(f)] and after 40 cycles [see Figure 7(c)] are used to observe amorphous carbon layers and the lattice fringes of ZnO and Co₃O₄ phases. Moreover, the HRTEM image of the ZnO/Co₃O₄@C electrode after 300 cycles [see Figure 7(d)] still retains a large amount of amorphous carbon, ZnO, and Co₃O₄ phases, indicating that ZnO/Co₃O₄@C hybrids show excellent reversibility during

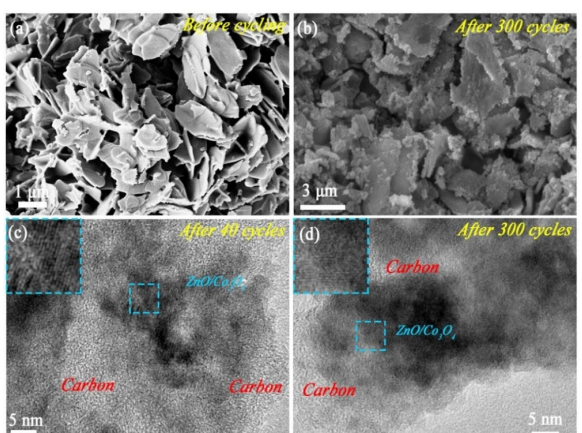


Figure 7. FESEM images of ZnO/Co₃O₄@C electrode a) before cycling and b) after 300 cycles. HRTEM images of ZnO/Co₃O₄@C electrode c) after 40 cycles and d) after 300 cycles.

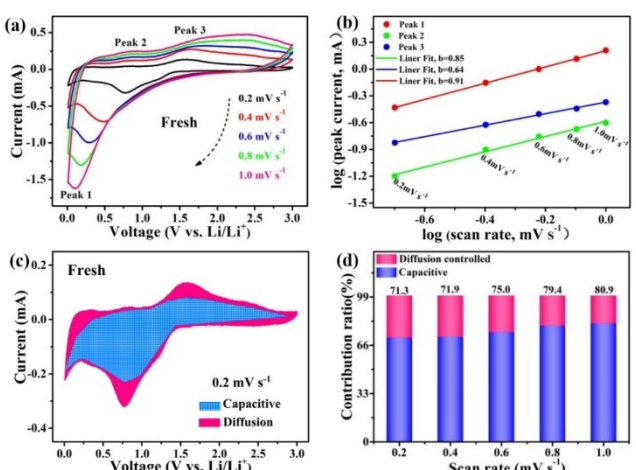


Figure 8. a) CV curves at various sweep rates, b) Analysis of *b*-value, c) The determination of capacitive and diffusion behaviors, and d) The ratios of the capacitive and diffusion-controlled contribution at different sweep rates for ZnO/Co₃O₄@C electrode.

lithiation/de-lithiation. The carbon layer helps to increase the conductivity of the electrode and provides many active sites for lithium storage.^[46–49] The polymer layer results in the additional capacity for the ZnO/Co₃O₄@C electrode through the “pseudocapacitive behavior” due to electrolyte degradation.

The pseudocapacitive behavior of the ZnO/Co₃O₄@C electrode is investigated using CV measurements from 0.2 to 1.0 mV s⁻¹. Figure 8(a) shows the CV curves at different sweep rates. There are relationships between the peak current (*i*) and scan rate (*v*) as Equations (6), (7).^[50,51]

$$i = a \cdot v^b \quad (6)$$

$$\log(i) = b \log(v) + \log(a) \quad (7)$$

where *a* and *b* are variable parameters, and the *b* value is represented by the slope of the log(*i*)-log(*v*) fitting lines. *b* ≤ 0.5, indicating the diffusion-controlled process; *b* = 0.6–1.0, indicating the capacitive process. Figure 8(b) shows the fitting results of log(*i*)-log(*v*) plots of the ZnO/Co₃O₄@C electrode. The *b* values corresponding to the cathodic peak (peak 1) and the anodic peaks (peaks 2 and 3) are 0.91, 0.85, and 0.64, respectively, suggesting that the charge storage of the ZnO/Co₃O₄@C electrode is dominantly controlled by the kinetics of capacitive characteristics. Then the capacitive contribution and diffusion-controlled contribution at a certain voltage are calculated by the following equations.^[51,52]

$$i(V) = k_1 v + k_2 v^{1/2} \quad (8)$$

$$i/v^{1/2} = k_1 v^{1/2} + k_2 \quad (9)$$

where *k₁v* and *k₂v^{1/2}* are the surface capacitive contribution and diffusion-controlled contribution, respectively. Therefore, when *k₁* and *k₂* are calculated, these contributions are capable of quantifying at a certain potential. Figure 8(c) exhibits the capacitive contribution of the ZnO/Co₃O₄@C electrode at a sweep rate of 0.2 mV s⁻¹. The total region is separated into two parts, the pink region stands for diffusion-controlled contribution and the blue region is capacitive contribution. The ratios of capacitive contribution are 71.3, 71.9, 75.0, 79.4, and 80.9% at 0.2, 0.4, 0.6, 0.8, and 1.0 mV s⁻¹, respectively (see Figure 8d). The higher capacitive contribution ratio shows that the ZnO/Co₃O₄@C hybrid has ultra-fast kinetics, which results in the extraordinary rate performance of the ZnO/Co₃O₄@C electrode.^[50–52]

3. Conclusions

In summary, the MOF-derived method was used to synthesize hollow mesoporous ZnO/Co₃O₄ hetero-nanostructures coated by carbon frameworks. Importantly, we studied the promotion effect of ZnO(110)/Co₃O₄(220) hetero-nanostructures at the atomic level. The ZnO/Co₃O₄@C exhibited a highly reversible pseudocapacitive lithium storage behavior, and it had a 71.3% capacitive contribution at the sweep rate of 0.2 mV s⁻¹. The

electrochemistry measurements results showed that ZnO/Co₃O₄@C hybrids possessed superior specific capacities with 1,758.3 mAh g⁻¹ after 370 cycles at 0.2 A g⁻¹ as well as 607.7 mAh g⁻¹ after 650 cycles at 5 A g⁻¹. Thus, this work provides a new idea for developing ZnO/Co₃O₄ heterostructures as energy storage devices. Besides, a new blueprint is created for developing efficient and fast lithium-ion energy storage systems.

Experimental Section

Preparation of ZnCo-ZIF, Zn-ZIF, and Co-ZIF

All reagents were not further purified. Generally, ZnCo-ZIF was synthesized by a simple precipitation method. Co(NO₃)₂·6H₂O and Zn(NO₃)₂·6H₂O (6 mmol totally) were dissolved into 50-mL deionized water. Then, 2-methylimidazole (C₄H₆N₂, 24 mmol) was distributed into 50-mL deionized water. The two solutions were uniformly mixed by stirring for 30 min. After that, the mixed solution was aged at room temperatures for 20 h. Finally, ZnCo-ZIF was collected by centrifugation, washed three times with deionized water, and dried at 60 °C for 12 h in a vacuum oven. Meanwhile, ZIF-67 (Co-ZIF) and ZIF-8 (Zn-ZIF) were synthesized by the above method without adding zinc or cobalt sources.

Preparation of porous hollow ZnO/Co₃O₄@C, ZnO@C, and Co₃O₄@C

First, the ZnCo-ZIF, Co-ZIF, and Zn-ZIF precursors were pre-sintered under argon (Ar) gas flow at 300 °C for 20 min at a heating rate of 1 °C min⁻¹. Afterward, the argon gas was turned off, and samples were heated to 400 °C at a heating rate of 0.2 °C min⁻¹ and kept in the air for 20 min. The ZnCo-ZIF, Co-ZIF, and Zn-ZIF precursors were converted into ZnO/Co₃O₄@C, Co₃O₄@C, and ZnO@C, respectively.

Materials characterization

The crystal structures of samples were studied by powder X-ray diffraction (XRD; Bruker D8 Advance, Cu_{Kα}, $\lambda=1.5406\text{ \AA}$). The surface morphology and energy dispersive X-ray (EDS) were characterized by the field scanning electron microscope (FESEM; ZEISS Gemini 500). The internal structure of samples was investigated by a transmission electron microscope (JEM-2100HR, 200 kV). The XPS was performed on Kratos Axis Ultra DLD. Thermogravimetric (TGA) analysis was conducted from 30 to 1100 °C in air. Brunauer-Emmett-Teller (BET) data and Raman patterns were collected on a surface area/porosity analyzer (Micromeritics, ASAP 2020) and a Raman spectrometer inVia, respectively. PL and UV-vis DRS spectra were obtained by a fluorescence spectrometer and CARY 300/PE Lambda 750S, respectively.

Electrochemical measurements

The electrochemical measurements were performed at room temperatures using CR 2032-type coin cells. The anode slurry was composed of N-methyl-pyrrolidone (NMP) as a solvent and active material (70 wt%), conductive carbon black (super P, 20 wt%), and Polyvinylidene fluoride (PVDF, 10 wt%) as the solute. This slurry was uniformly coated on copper foil and then dried at 60 °C for 12 h. The mass loading of active materials on Cu substrates is ~1 mg. The half-cells were manufactured in an argon-filled glove

box using 1 M LiPF₆ in a mixture of ethylene carbonate and dimethyl carbonate (EC: DMC = 1:1 vol.%) as the electrolyte, Celgard 2400 membrane as a separator, and lithium metal as a counter electrode, respectively. The galvanostatic charge/discharge tests of half-cells were conducted in the potential range of 0.01–3.0 V (vs. Li⁺/Li) using the LAND cell test system at room temperatures. Cyclic voltammetry (CV) and the electrochemical impedance spectral (EIS) experiment were performed using an electrochemical analyzer (CHI 660D). The Mott-Schottky experiments were conducted against Ag/AgCl as the reference electrode.

DFT calculation

The first-principle calculations based on density functional theory (DFT) were performed through Cambridge Sequential Total Energy Package (CASTEP) with a plane-wave basis for the electronic wave functions. Ultrasoft pseudopotentials were used to treat the interaction between the core electrons and the valence electrons. Theoretical calculations based on local DFT were considered a beneficial tool to analyze the properties of surface structures. The exchange and correlation interactions were dealt by the GGA-PBE function. The plane wave cutoff was set as 450.0 eV. The k-points of 5×5×3 and 3×3×3 were applied to bulk ZnO and Co₃O₄ using the Monkhorst-Pack scheme.

Brillouin-zone integration was performed using a 1×2×1 Monkhorst-Pack grid for the ZnO(110)/Co₃O₄(220) heterojunction structure. A DFT-D2 method was adopted in all calculations to account for the van der Waals interactions between the substrates. The LDA+U method with Hubbard $U=2.0$ eV was introduced to transition metal oxides. Spin-polarized DFT calculations were performed to account for the magnetic nature of Co atoms. The LST/QST method was used to search the transition state and four or six images inserted in between two stable states.

Acknowledgements

This work was supported by the Key Project of Guangdong Province Nature Science Foundation (No. 2017B030311013) and the Scientific and Technological Plan of Guangdong Province, Guangzhou and Qingyuan Cities, China (Nos. 2019B090905005, 2019B090911004, 2017B020227009, 201804010169, 2019DZX008, 2019A004, 2020DZX014), as well as the Innovation Project of Graduate School of South China Normal University (No. 2019LKXM004).

Conflict of Interest

The authors declare no conflict of interest.

Keywords: DFT calculation · lithium-ion batteries · interfacial effect · ZnO(110)/Co₃O₄(220) hetero-nanostructure

- [1] F. Zhang, L. Qi, *Adv. Sci.* **2016**, *3*, 1600049.
- [2] S. Yuan, Z. Guo, L. Wang, S. Hu, Y. Wang, Y. Xia, *Adv. Sci.* **2015**, *2*, 1500071.
- [3] J. Liang, X. Y. Yu, H. Zhou, H. B. Wu, S. X. W. Ding, *Angew. Chem. Int. Ed.* **2014**, *53*, 12803–12807; *Angew. Chem.* **2014**, *126*, 13017–13021.

- [4] G. Z. Fang, J. Zhou, C. W. Liang, A. Q. Pan, C. Zhang, Y. Tang, X. P. Tan, J. Liu, S. Q. Liang, *Nano Energy* **2016**, *26*, 57–65.
- [5] Q. Xie, Y. Ma, X. Wang, D. Zeng, L. Wang, L. Mai, D. L. Peng, *ACS Nano* **2016**, *10*, 1283–1291.
- [6] J. Zhan, K. Wu, X. Yu, M. Yang, X. Cao, B. Lei, D. Pan, H. Jiang, M. Wu, *Small* **2019**, *15*, 1901083.
- [7] H. Kong, C. Yan, C. Lv, J. Pei, G. Chen, *Mater. Chem. Front.* **2019**, *3*, 909–915.
- [8] L. Fang, Z. Lan, W. Guan, P. Zhou, N. Bahlawane, W. Sun, Y. Lu, C. Liang, M. Yan, Y. Jiang, *Energy Storage Mater.* **2019**, *18*, 107–113.
- [9] C. Guo, W. Zhang, Y. Liu, J. He, S. Yang, M. Liu, Q. Wang, Z. Guo, *Adv. Funct. Mater.* **2019**, *29*, 1901925.
- [10] H. Zhou, Y. Qu, T. Zeid, X. Duan, *Energy Environ. Sci.* **2012**, *5*, 6732.
- [11] J. Low, J. Yu, M. Jaroniec, S. Wageh, A. A. Al-Ghamdi, *Adv. Mater.* **2017**, *29*, 1601694.
- [12] W. T. Li, K. N. Shang, Y. F. Zhu, R. H. Zeng, L. Z. Zhao, *Electro. Acta* **2015**, *174*, 85–991.
- [13] H. Chen, L. Deng, S. Luo, X. Ren, Y. Li, L. Sun, P. Zhang, G. Qiang, Y. Gao, *J. Electrochem. Soc.* **2018**, *16*, A3932.
- [14] G. Fang, J. Zhou, Y. Cai, S. Liu, X. Tan, A. Pan, S. Liang, *J. Mater. Chem. A* **2017**, *5*, 13983–13993.
- [15] D. Zhu, F. Zheng, S. Xu, Y. Zhang, Q. Chen, *Dalton Trans.* **2015**, *44*, 16946–16952.
- [16] J. Shi, F. Qiu, W. Yuan, M. Guo, Z. Lu, *Chem. Eng. J.* **2021**, *403*, 126312.
- [17] K. Ao, Q. Wei, W. A. Daoud, *ACS Appl. Mater. Interfaces* **2020**, *12*, 33595–33602.
- [18] J. Li, W. Xia, J. Tang, H. Tan, J. Wang, Y. V. Kaneti, Y. Bando, T. Wang, J. He, Y. Yamauchi, *Nanoscale Horiz.* **2019**, *4*, 1006–1013.
- [19] S. Zhang, W. Xia, Q. Yang, Y. V. Kaneti, X. Xu, S. M. Alshehri, T. Ahamad, Md. S. A. Hossain, J. Na, J. Tang, Y. Yamauchi, *Chem. Eng. J.* **2020**, *396*, 125154.
- [20] H. Xu, K. Ye, K. Zhu, Y. Gao, J. Yin, J. Yan, G. Wang, D. Cao, *Inorg. Chem. Front.* **2021**, *8*, 2788–2797.
- [21] S. Zhang, Q. Yang, X. Xu, X. Liu, Q. Li, J. Guo, N. L. Torad, S. M. Alshehri, T. Ahamad, Md. S. A. Hossain, Y. V. Kaneti, Y. Yamauchi, *Nanoscale* **2020**, *12*, 15611–15619.
- [22] X. F. Lu, Y. Chen, S. Wang, S. Gao, X. W. D. Lou, *Adv. Mater.* **2019**, *31*, e1902339.
- [23] K. Wang, D. Liu, P. Deng, L. Liu, S. Lu, Z. Sun, Y. Ma, Y. Wang, M. Li, B. Y. Xia, C. Xiao, S. Ding, *Nano Energy* **2019**, *64*, 103954.
- [24] Y. Gong, Z. Xu, H. Pan, Y. Lin, Z. Yang, X. Du, *J. Mater. Chem. A* **2018**, *6*, 5098–5106.
- [25] P. Ge, S. Li, L. Xu, K. Zou, X. Gao, X. Cao, G. Zou, H. Hou, X. Ji, *Adv. Energy Mater.* **2019**, *9*, 1803035.
- [26] Y. Zhao, W. Wang, M. Chen, R. Wang, Z. Fang, *CrystEngComm* **2018**, *20*, 7266–7274.
- [27] H. Wang, K. Xie, Y. You, Q. Hou, K. Zhang, N. Li, W. Yu, K. P. Loh, C. Shen, B. Wei, *Adv. Energy Mater.* **2019**, *9*, 1901806.
- [28] M. Rashad, M. Rüsing, G. Berth, K. Lischka, A. Pawlis, *J. Nanomater.* **2013**, *10*, 1–6.
- [29] S. G. Zhang, X. W. Zhang, X. Liu, Z. G. Yin, H. L. Wang, H. L. Gao, Y. J. Zhao, *Appl. Phys. Lett.* **2014**, *104*, 121109.
- [30] T. Wu, M. Jing, Y. Liu, X. Ji, *J. Mater. Chem. A* **2019**, *7*, 6439–6449.
- [31] Y. M. Sun, X. L. Hu, W. Luo, Y. H. Huang, *ACS Nano* **2011**, *5*, 7100–7107.
- [32] E. Samuel, B. Joshi, M. W. Kim, Y. I. Kim, S. Park, T. G. Kim, M. T. Swihart, S. S. Yoon, *J. Power Sources* **2018**, *395*, 349–357.
- [33] S. L. Xiong, J. S. Chen, X. W. Lou, H. C. Zeng, *Adv. Funct. Mater.* **2012**, *22*, 861–871.
- [34] R. B. Wu, X. Q. Qian, K. Zhou, J. Wei, J. Lou, M. Ajayan, *ACS Nano* **2014**, *8*, 6297–6303.
- [35] D. Zhu, F. Zheng, S. Xu, Y. Zhang, Q. Chen, *Dalton Trans.* **2015**, *44*, 16946–52.
- [36] J. Li, S. Hou, T. Z. Liu, L. K. Wang, C. Mei, Y. Y. Guo, L. Z. Zhao, *Chem. Eur. J.* **2020**, *26*, 2013–2024.
- [37] D. Wang, J. Yang, X. Li, D. Geng, R. Li, M. Cai, X. Sun, *Energy Environ. Sci.* **2013**, *6*, 2900–2906.
- [38] S. J. Rezvani, R. Gunnella, A. Witkowska, F. Mueller, M. Pasqualini, F. Nobili, A. D. Cicco, *ACS Appl. Mater. Interfaces* **2017**, *9*, 4570–4576.
- [39] C. Yan, C. Lv, Y. Zhu, G. Chen, J. Sun, G. Yu, *Adv. Mater.* **2017**, *29*, 1703909.
- [40] T. G. Kim, E. Samuel, B. Joshi, C. W. Park, M. W. Kim, M. T. Swihart, S. S. Yoon, *J. Alloys Compd.* **2018**, *766*, 331–340.
- [41] Z. Y. Wang, D. Y. Luan, S. Madhavi, Y. Hu, D. Lou, *Energy Environ. Sci.* **2012**, *5*, 5252–5256.
- [42] Q. Xia, H. Zhao, Z. Du, Z. Zeng, C. Gao, Z. Zhang, X. Du, A. Kulka, K. Świerczek, *Electro. Acta* **2015**, *180*, 947–956.
- [43] F. Zou, Y. M. Chen, K. W. Liu, Z. T. Yu, W. F. Liang, M. Gao, Y. Zhu, *ACS Nano* **2015**, *10*, 377–386.
- [44] J. C. Guo, Q. Liu, C. S. Wang, M. R. Zachariah, *Adv. Funct. Mater.* **2012**, *22*, 803–811.
- [45] S. Hou, P. Wang, Y. P. Li, F. Pang, M. Liu, Y. Z. Luo, L. Z. Zhao, *Appl. Surf. Sci.* **2019**, *476*, 959–965.
- [46] H. Yue, Z. Shi, Q. Wang, T. Du, Y. Ding, J. Zhang, N. Huo, S. Yang, *RSC Adv.* **2015**, *92*, 75653–75658.
- [47] Y. P. Li, C. H. Yang, F. H. Zheng, X. Ou, Q. C. Pan, Y. Z. Liu, G. Wang, *J. Mater. Chem. A* **2018**, *37*, 17959–17966.
- [48] Y. P. Li, W. T. Zhong, C. H. Yang, F. H. Zheng, Q. C. Pan, Y. Z. Liu, G. Wang, X. H. Xiong, M. L. Liu, *Chem. Eng. J.* **2019**, *358*, 1147–1154.
- [49] H. Sun, G. Xin, T. Hu, M. Yu, D. Shao, X. Sun, J. Lian, *Nat. Commun.* **2014**, *5*, 4526.
- [50] J. Wang, J. L. Polleux, J. Lim, B. Dunn, *J. Phys. Chem. C* **2017**, *111*, 14925–14931.
- [51] D. Ni, W. Sun, Z. Wang, Y. Bai, H. Lei, X. Lai, K. Sun, *Adv. Energy Mater.* **2019**, *9*, 1900036.
- [52] G. Fang, Z. Wu, J. Zhou, C. Zhu, X. Cao, T. Lin, S. Liang, *Adv. Energy Mater.* **2018**, *8*, 1703155.

Manuscript received: June 5, 2021

Revised manuscript received: August 9, 2021

Accepted manuscript online: August 22, 2021

Version of record online: October 4, 2021